2007

# Quantitative method for measurement of the Goos-Hanchen effect based on source divergence considerations

Jeffrey F. Gray
*University of New Orleans*

Ashok Puri
*University of New Orleans*



Recommended Citation
Phys. Rev. A 75 063826 (2007)

# Quantitative method for measurement of the Goos-Hanchen effect based on source divergence considerations

Jeffrey F. Gray
*Department of Electrical Engineering, University of New Orleans, New Orleans, Louisiana 70148, USA*

Ashok Puri*
*Department of Physics, University of New Orleans, New Orleans, Louisiana 70148, USA*
(Received 13 July 2005; published 26 June 2007)

In this paper we report on a method for quantitative measurement and characterization of the Goos-Hanchen effect based upon the real world performance of optical sources. A numerical model of a nonideal plane wave is developed in terms of uniform divergence properties. This model is applied to the Goos-Hanchen shift equations to determine beam shift displacement characteristics, which provides quantitative estimates of finite shifts near critical angle. As a potential technique for carrying out a meaningful comparison with experiments, a classical method of edge detection is discussed. To this end a line spread Green's function is defined which can be used to determine the effective transfer function of the near critical angle behavior of divergent plane waves. The process yields a distributed (blurred) output with a line spread function characteristic of the inverse square root nature of the Goos-Hanchen shift equation. A parameter of interest for measurement is given by the edge shift function. Modern imaging and image processing methods provide suitable techniques for exploiting the edge shift phenomena to attain refractive index sensitivities of the order of $10^{-6}$, comparable with the recent results reported in the literature.

DOI: 10.1103/PhysRevA.75.063826 PACS number(s): 42.25.−p, 42.25.Gy, 78.20.Bh

## INTRODUCTION

In 1947 Goos and Hanchen [1] verified an earlier conjecture by Newton [2] that light beams incident at an internal reflection boundary experienced lateral shifts along the plane of the interface before being reflected. This shift is now known as the Goos-Hanchen shift. The standard equations for calculating the shifts for both parallel and perpendicular states of polarization [3] are functionally dependent on the angle of incidence and the ratio of index of refraction between the two mediums. In the standard form the equations describe the behavior of ideal light sources, however; the nonideal nature of real world sources must be included for proper interpretation of observed results.

The measured Goos-Hanchen shift near critical angle was finite [1] but expressions for shift reported in literature diverged near critical angle. A detailed earlier review of theory and experiment was given by Lotsch [4]. Researchers including deBroglie [5], Troup [6], Horowitz and Tamir [7], Puri and Birman [8], and Antar and Boerner [9], among others have proposed methods of approximating the nonideal nature of the phenomena and have developed models for finite Gaussian beam shift near critical angle. The general observation that maximum shift actually occurs slightly off of the critical angle is supported by the Gaussian beam models. Contemporary efforts in GH shift have focused on the shift induced in the TM states of Gaussian beams under plasmon surface resonance [10–12].

Our purpose in this paper is to investigate a parallel quantitative method that provides a deeper understanding of nonideal plane wave interaction at internal reflection near critical angle. First, we introduce a numerical modeling approach and demonstrate compatibility with prior science (see Fig. 3 and explanations thereafter). Then we evaluate the resulting dispersion relationships [Eq. (A15) generalized to Eq. (7)] which lead to the nonmonotonic behavior of the mean shift properties. We find that a class of measurement methods exists which exploit the edge-shift, or minimum shift, phenomena exhibited along the shadow lines of step apertures. Most prior experimental efforts have relied on detection of mean shift of beam spots and there is near universal agreement that maximum mean shift occurs at angles slightly offset from critical angle.

The method laid down in this effort identifies an alternate measurable parameter, the aperture edge shift [Eq. (A4)], which exhibits maximum deflection at critical angle and maximum sensitivity to angular alignment at the critical angle [see Appendix B, Eq. (B4)]. The edge shift function (A4) is monotonic on either side of the critical angle as its derivative (B4). Such behavior is well suited for precise location of critical angle leading to improved resolution in refractive index measurement. This treatment leads to a mathematical formulation showing that control of beam divergence is a principal limiting factor in enhancing Goos-Hanchen shift near critical angle. This paper also defines criteria for comparing observed beam shift data with theoretical results. The problem requires that we examine the definition of beam shift and discriminate the classical method of edge detection from the mean shift predictions of the equations.

In this paper uniform divergence model is used as an approximation in description of the non-ideal nature of a real optical source. Many additional factors, e.g., irregularities in aperture, nonuniform source distribution, alignment, and scattering, among others, contribute toward real source anomalies. Thus real optical source is not limited by only

*Email address: apuri@uno.edu

 

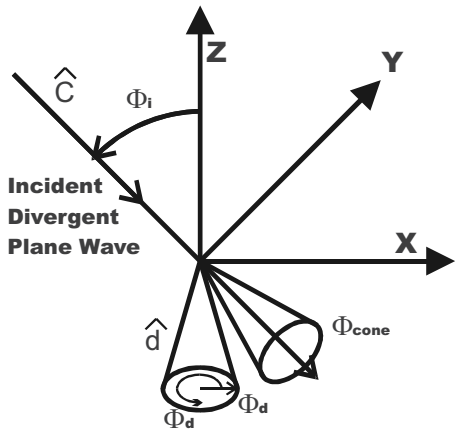


FIG. 1. Divergence geometry.

uniformly divergent waves. However, by establishing a standard plane-wave source based upon well controlled beam qualities and divergences we can set a nominal baseline from which, in principle, other source deviations can be extracted by interpreting measured deviations from the nominal response curves.

The present work is motivated by both fundamental and practical considerations. Measurement of refractive index variation has strong potential for diagnosis of efficiency in liquid and gas mixing applications, measurement of homogeneity of solid materials, and noninvasive contamination testing. In addition the resulting form also provides diagnostic information that may be useful in a broad range of physical applications including optical source collimation and alignment considerations.

## APPROACH

All natural and manmade sources emanate from finite size sources and possess some form of natural divergence. Our goal is to model the natural divergence and derive a Green's function for the distributed Goos-Hanchen effect over the cone of divergence that results from consideration of the finite dimensions of the source.

Consider a plane wave incident on an internal reflection surface with a uniform cone of divergence as shown in Fig. 1. To define the general impulse response that occurs at each individual point of the reflection interface, we must first determine the amount and direction of light arriving at the interface. This is the collimation of the wave, and we generalize our definition to that of a uniform circular source with finite dimensions at some distance from the interface. Without loss of generalization we can reflect the incoming convergent cone of light to an outgoing diverging cone. If we define the *Y*-*Z* plane as the interface plane, we can deconstruct the incoming beam into two vectors, one vector along the mean direction of the wave and a second vector representing the divergence cone aligned to the *z* axis. This provides an elegant dot-product representation of the divergent wave that can be applied directly to the Goos-Hanchen shift equation.

When this model is applied to the shift equations, we find a variation in the individual component responses of the wave, depending on the degree to which the divergence causes the incidence angles of the individual components to deviate from critical angle. Only a small portion sees significant shifts and virtually none of the beam sees the infinite shift that occurs along the singularity line.

Uniform divergence means that wave propagation is uniform within a fixed theta/phi cone of divergence. At any point in the beam, light rays propagate within a small uniform angular deviation from the beam propagation vector. If we choose the *z* axis normal to the optical interface plane then the divergence cone can be expressed in vector form as $\hat{d}$ and the incident plane wave can be expressed as $\hat{c}$ by the following vectors, where phi and theta are the polar angles defining the divergence cone:

$$\hat{d} = [\sin(\theta_d)\sin(\phi_d), \sin(\theta_d)\cos(\phi_d), -\cos(\theta_d)],$$

$$\hat{c} = [\sin(\theta_i), 0, -\cos(\theta_i)]. \tag{1}$$

Also $\cos(\theta_r) = (\hat{c} \cdot \hat{d})$.

This represents the incidence angle of each component within the divergence cone. By recasting the Goos-Hanchen equation into a cosine form we can directly apply the dot product and obtain a representation of the shift equation in terms of the divergence cone angles

$$D_\perp = \frac{\lambda}{\pi} \frac{\sin(\theta_c)}{\sqrt{\sin^2(\theta_c) - \sin^2(\theta_i)}}$$

becomes

$$D_\perp = \frac{\lambda}{\pi} \frac{\sin(\theta_c)}{\sqrt{\cos^2(\theta_r) - \cos^2(\theta_c)}}.$$

The incidence subscript $(i)$ here is changed to a refraction subscript $(r)$ indicating we have shifted from a plane wave model to a divergence model.

Expanding the dot product, $\cos(\theta_r) = (\hat{c} \cdot \hat{d})$, we obtain

$$\cos(\theta_r) = \sin(\theta_c + \delta)\sin(\theta_d)\sin(\phi_d) + \cos(\theta_c + \delta)\cos(\theta_d). \tag{2}$$

The delta angle $(\delta = \theta_i - \theta_c)$ in Eq. (2) allows for deviation of the incident angle around the critical angle.

In this uniform divergence model the Goos-Hanchen equation singularities lie along a theta-phi contour in the divergence cone that can be found from Eq. (2) for all values of delta less than the divergence of the beam. The resulting contours as a function of $\delta$ are concentric long radius (compared to $\theta_d$) circular arcs. A simplified representation is given as follows:

$$\sin(\phi_d) = \frac{\cos(\theta_r) - \cos(\theta_c + \delta)\cos(\theta_d)}{\sin(\theta_c + \delta)\sin(\theta_d)}, \tag{3}$$

where $\theta_r = \theta_c$ near the critical angle.

## ANALYTICAL/NUMERICAL RESULTS

The shift function plotted as height over the circle of the divergence cone is shown in Fig. 2 with a delta angle of 1/2

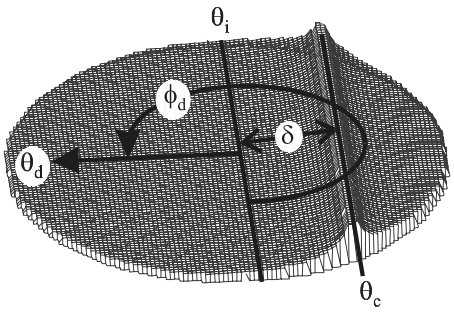


FIG. 2. Goos-Hanchen shift distributions over the cone of divergence.

of the divergence angle of the beam. The singularity contour is truncated for clarity and overlaid for labeling.

Mean beam offset can now be calculated from standard centroid techniques in a theta, phi polar representation over the cone of divergence:

$$D_{\text{mean}} = \frac{\int\int D_{\perp}(\theta_d, \phi_d)\theta_d d\theta_d d\phi_d}{\int\int \theta_d d\theta_d d\phi_d}. \tag{4}$$

The integral is further divided into two separate components, the portions of the beam incident above and below the critical angle. Above the critical angle totally reflection occurs, but below the critical angle the Fresnel reflectance coefficients that drop off rapidly must be applied. The observed shift will be a combination of the intensity contributions from the two components. The reflection coefficient drop-off in the region below critical angle is observed to cause asymmetry in the mean displacement versus delta angle curves.

Figure 3 shows the relationships between the delta angle, the beam divergence and the predicted mean shifts of the beam by the model. The shift curve is nearly flat at critical angle and does not substantially decline until delta approaches the divergence angle. At small divergences, the shift rolls off slowly below critical angle and drops exponentially when delta exceeds the divergence angle. At larger divergences the shift will rise slowly and reach maximum near the divergence angle before dropping exponentially. This case is for the perpendicular polarization at incidence angles below critical. For delta angles larger than the divergence angle, the mean shift response asymptotically approaches the classical equation of Artmann's ideal response curves.

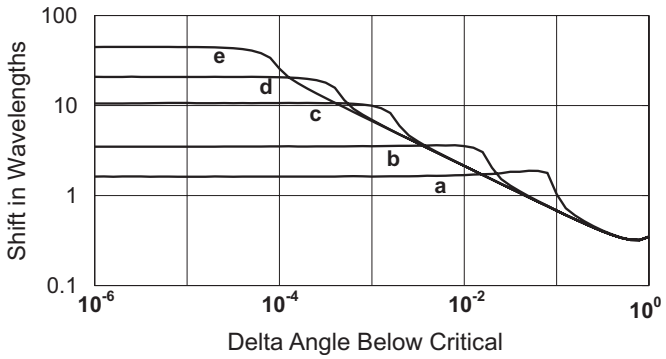


FIG. 3. Mean shift vs delta angle and divergence below critical angle. Lines (a)–(e) correspond to divergences of 0.01, 0.002, 0.0002, 0.0005, and 0.0001, respectively. The common convergence line corresponds to Artman's inverse square root equation.

It is worth noting that similar finite beam shifts at critical angle have been reported in paraxial, or angular spectrum, approximation [7,8]. The conjecture of Horowitz and Tamir [7] that nongaussian wave behavior for mean shift will be similar but not identical to Gaussian beam behavior is supported by our numerical models

The equation for mean beam shift (4) can be misleading when used in interpretation of experimental results. Due to the microscopic size and asymmetric shape of the dominant shift effect, mean displacement is difficult to measure accurately with imaging methods. Traditional edge detection methods typically locate the maximum slope of the image intensity profile at the edge. In the divergence model the maximum slope occurs at the leading edge of the shifted image, permitting a direct calculation of the minimum shift the divergence cone sees as follows:

$$D_{\perp \text{edge}} = \frac{\lambda}{\pi} \frac{\sin(\theta_c)}{\sqrt{|\sin^2(\theta_{\max}) - \sin^2(\theta_c)|}}. \tag{5}$$

$\theta_{\max} - \theta_c$ is the maximum deviation of the divergence cone from the critical angle and establishes the minimum shift.

The impulse response shift is found by numerical methods as a histogram of the Goos-Hanchen shift over the cone of divergence at a single point. This will define the light wave behavior for a single point input. Typically we would describe this in terms of a point-spread function. But since the shift is most readily seen near linear edges, the logical extension to a line spread function is more appropriate for our purposes.

This is because in real applications the off-axis or longitudinal shifts for small divergences relative to the angle of incidence are negligible in comparison to the lateral shift. Exceptions to this rule must be considered when the divergence angle becomes a significant percentage (>5%) of the angle of incidence.

The resulting Green's function can then be convolved over the plane wave incidence region (i.e., over slit width) to provide an estimate of the output intensity profile for total beam behavior near lateral edges. Figure 4 shows a typical line spread function for a .01 radian divergence beam. The sharp leading edge of the curve that is the most recognizable feature of the graph from an image processing perspective, locates the minimum displacement given in Eq. (5).

A nearly exact expression for the line spread function is derived in Appendix A [Eq. (A6)] of this paper

$$I(D_{\perp}) = \frac{2I_0}{\lambda\theta_d^2}\sqrt{\theta_d^2 - d^2}\sqrt{\cot(\theta_i)}\sqrt{(\delta - d)^3}, \tag{6}$$

where $d = \delta - \lambda^2/\pi^2 D_{\perp}^2 2\cot(\theta_i)$. Equation (6) is valid for $\theta_i \gg \delta$ and $\delta \ll 1$. When $\delta \leqslant \theta_d$ a simpler expression for the line

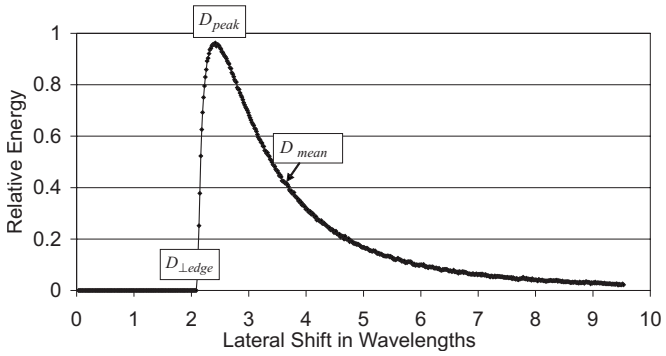


FIG. 4. Goos-Hanchen line spread function for $\delta=0$ showing locations of edge, peak, and mean shifts.

spread function seen in Fig. 4 is given by a closed form approximation [see Eq. (A13)].

$$I_{\mathrm{LSF}} = \frac{I_0}{\pi\theta_d}\sqrt{[\sin(\theta_d+\delta)]^3}\sqrt{2\cot(\theta_i)} \times \sqrt{\left(\frac{D_{\perp\mathrm{edge}}}{x}\right)^a - \left(\frac{D_{\perp\mathrm{edge}}}{x}\right)^b}\, x \geqslant D_{\perp\mathrm{edge}}. \quad (7)$$

The coefficients $a$ and $b$ are empirically derived, $x$ is the lateral shift value, and $D_{\perp\mathrm{edge}}$ is found from Eq. (5). At critical angle the values of $a$ and $b$ are ~6 and ~10, respectively, for the leading components of waves with divergences less than 0.01 radians. This derives directly from Eq. (A12). As delta increases from zero to the divergence angle, the values of $a$ and $b$ tend to converge toward 8 in the approximate form. The analytical form with the harmonic oscillator terms is given in Eq. (A15a). For ease in numerical calculations the approximate form of Eq. (7) gives results within 1% for appropriate values of $a$ and $b$ as verified by numerical modeling.

The line-spread function given in Eqs. (6) and (7) and shown in Fig. 4 represents one of the two portions of the complete line spread function. If the beam is incident at the critical angle and the divergence is small enough to minimize the reflectance losses, the leading and trailing shift functions will be nearly identical and the total shift will normalize to the given results. When the incidence angle of beam varies between the critical angle and the divergence angle, the leading and trailing components will be different and the total line spread function will be a sum of the two contributions. For divergences of 0.01 radians and greater, the reflectance factors in the trailing components become significant and the trailing component graph will be shortened and reduced in overall magnitude. Equation (7) is modified to reflect the distinction between the leading and trailing components resulting in Eq. (8) that is the line spread Green's function for the divergence model when $\delta$ is less than or equal to the divergence angle. The square root of the negative quantity in the trailing component accounts for the phase difference between leading and trailing spots. Figure 5 shows a typical plot of split components of Eq. (8) for a divergence of 0.001 radians and a delta of 0.0001 radians:

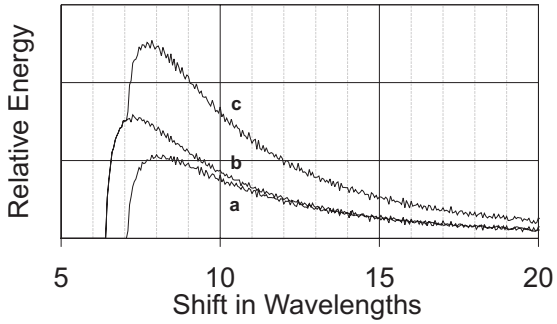


FIG. 5. Goos-Hanchen line spread function for two split components. Lines (a)–(c) represent the trailing, leading, and sum of leading and trailing components, respectively. Divergence is 0.001 radians and delta angle ($\delta$) is 0.0001 radians.

$$I_{\mathrm{LSF}} = \frac{I_0}{\pi\theta_d}\sqrt{[\sin(\theta_d+\delta)]^3}\sqrt{2\cot(\theta_i)} \times \sqrt{\left(\frac{D_{\perp\mathrm{edge}}}{x}\right)^{a_L} - \left(\frac{D_{\perp\mathrm{edge}}}{x}\right)^{b_L}} + \frac{I_0}{\pi\theta_d}\sqrt{[\sin(\delta-\theta_d)]^3}\sqrt{2\cot(\theta_i)} \times \sqrt{\left(\frac{D_{\perp\mathrm{edge}}}{x}\right)^{a_T} - \left(\frac{D_{\perp\mathrm{edge}}}{x}\right)^{b_T}}. \quad (8)$$

If we combine the findings from Eqs. (5)–(7) and the graphical results seen in Figs. 3–5 it is possible to extend our observations towards practical applications of the Goos-Hanchen shift. Additionally, a strong dependence of the shift on the ratio of refractive indices completes a design criterion for a potential white light imaging interferometer based on Goos-Hanchen shift.

Figure 6 shows that large shifts are obtainable by careful control of the divergence angle. Note that the divergence is a limiting factor for observable shifts. Figure 6 also shows that the shifts can be amplified by reducing the ratio of refractive indices at the internal reflection boundary. The graph suggests that large single reflection shifts can be obtained by

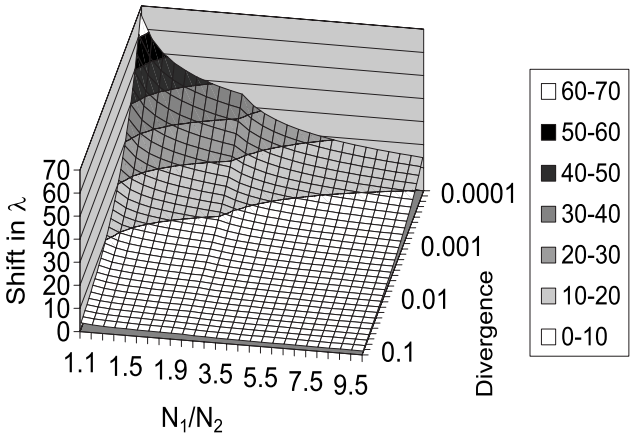


FIG. 6. Mean shift sensitivities as a function of divergence and refractive index ratios. Refractive index scale changes at 2 from 0.1 per division to 0.5 per division.

controlling these two parameters. This method can also increase the reliability of devices that depend on the shift effect.

Furthermore, the functional form of the line-spread function appears to be well suited to interferometric purposes and may well lend itself to extensions of the phase shifting methods that have dramatically improved sensitivity of interferometry. Efficient design methods might be able to produce spatially distributed interferograms where localized variations in index of refraction appear as fringe line contours.

## MEASUREMENT DESIGN CONSIDERATIONS

In traditional photographic experiments, a single shift value is extracted for a single rectilinear mask aperture. This method of single edge detection can be directly extended to simultaneous measurement of multiple adjacent edges when digital image capture and analysis is employed. Additionally, multiple adjacent apertures can then be added, creating an array of sampling points. The individual apertures can be measured and analyzed independently to provide a means for measuring localized variations in refractive index or they can be combined for obtaining higher sensitivity to a nonlocalized mean refractive index. This allows for two measurements regimes to be performed over a sensing area rather than a single sensing line.

Prior method of implementing rectilinear masks require improvement and we suggest the use of stripped single mode optical fibers or the use of etched chrome-on-glass Ronchi rulings. The former possess very sharp edges but are difficult to position in uniform arrays. The latter can be fabricated in precise two-dimensional arrays but possess diffraction limited edge roughness. Ronchi rulings are also suited for mounting onto piezoelectric positioning devices for positional stepping similar to the "jitter" camera used in superresolution sampling [12].

In a design consideration for adjacent apertures, it must be noted that slit width and separation dimensions are affected by crosstalk. To minimize the crosstalk, Fig. 4 can be used as a design guide for slit spacing and slit width. A recommended starting point would be to have both the slit width and slit spacing close to the mean shift shown in Fig. 4. The limiting values of slit width could be comparable to edge shift, and slit separation could be as much as twice the mean shift. Design trade-off must be considered relating to working source divergences, e.g., low source divergences will lead to higher slit width and spacing. This will reduce diffraction effects. However, higher divergence will lead to $\lambda$ size shifts, which will increase diffraction effects. Thus slit widths of the order of wavelength will increase diffraction effects which are not desirable, however slit widths of the order 10 $\lambda$ will reduce diffraction effects and are desirable.

In addition, design trade-offs must be considered relating the working source divergence and desired sampling densities when the method is used for area coverage. Larger source divergences allow for denser sampling of an area but with a resultant reduction in overall sensitivity. Achieving higher sensitivity requires greater spread between sampling points in a gridded aperture configuration to account for the increases in lateral displacement near critical angle. Sources of one milliradian divergence for example will produce shifts nearly equivalent to single pixel widths of conventional CCD-imaging chips.

Multiple aperture methods are well suited for measuring distributions of refractive index variation over a sensing area. Very precise measurements of localized variations can be combined with distributed analysis methods for more accurate determination of mean refractive index.

## COMPARISON OF DIVERGENT METHOD WITH CURRENT RESEARCH

Researchers have reported attaining sensitivities of $10^{-6}$ index variation measurement [13]. For comparison purposes we can project the theoretical operating parameters for a divergent measurement system including source divergence, refractive index ratio, single vs multiple reflections, diffraction limited imaging, subpixel feature extraction, over sampling, and super-resolution.

First, the single reflection, shift for a 0.001 radian beam is near $6\lambda$ at an operating refractive index ratio of 1.5. For a 1/3 in. CCD imager with a pixel size of 4 $\mu$m and an optical magnification of 4:1, a single pixel size is on the order of magnitude of $2\lambda$ in the green. To detect a change of $10^{-4}$ in refractive index of the air would require resolving $D_{\text{edge}}$ to 0.15 pixels. This level of detection has been achieved [14]. Details of sensitivity of refractive index derivation are given in Appendix B. To detect changes of $10^{-5}$ in $n$ would similarly require 0.015 pixels discrimination, which has also been attained with edge detection methods. In a CCD array with the axis of the aperture aligned to the axis of the pixel through the imaging system, multiple parallel rows will see a stable sampling population allowing the use of 100 parallel sample rows in both the shifted and unshifted portions of the wavefront to provide the additional resolving power to attain $10^{-6}$ resolution on $n$. Furthermore, sampling of parallel rows of apertures, improving the divergence of the source, and multiple reflections are all possible techniques to further extend the method.

## CONCLUSIONS

The effect of source divergence on Goos-Hanchen shift has been studied and numerically evaluated to predict the real world performance of observable sources. A line spread function has been found in graphical form, derived in analytical form, and reduced to a simplified closed form approximation. The model results support prior observations (finite shifts at critical angle [7,8]) and should provide techniques for adequate interpretation of experimental shift measurements. The paper addresses the possible sources of contradictions that may arise in the experimental observations. First, variations in beam quality, i.e., divergence, can produce differing results. Second, interpretation of beam shift is highly dependent on the measured beam shift features. Mean shift predicted by the equations is significantly different from edge shift observation. As shown in Fig. 4, edge shift is nearly 60% of the mean shift. Maximum shift location de-

pends on magnitude of divergence and which side of the critical angle that the incidence angle lays.

Our findings are summarized as follows. (1) The divergence model is compatible with prior results from Gaussian beam analysis. (2) Source divergence for plane waves is similar, but not identical to beam waist parameter for Gaussian beam. (3) Introduction of beam divergence leads to simplified expression for spatial dispersion. (4) Divergence is the primary limiting parameter for enhancing shift magnitudes. (5) A measurement parameter based upon edge shift behavior has been defined and is shown to be well behaved and highly sensitive to angular shift and refractive index variation. The edge parameter shows monotonic behavior on either side of critical angle, is independent of spot splitting, and has a monotonic slope which is discontinuous at critical angle. (6) Current technological capabilities exist to support precise imaging and edge localization.

## FOLLOW-UP EFFORTS

Follow-up efforts are underway to experimentally verify the models presented in this paper. Our next paper will present a simple experimental setup identifying the major components for performing baseline measurements. The goal is both to obtain a high precision shift measurement and to measure the edge rise profile predicted by the line spread function. We will also show that the imaged quantity is convolution of the line spread function with the aperture. The spatial nature of the divergence model and the apertures make the overall process more meaningful when performed and interpreted in the spatial domain. Ultimately, we hope to experimentally show that the spatial domain approach for planes waves produces similar but not identical results to the FT approach for Gaussian beams.

## APPENDIX A: MATHEMATICAL DERIVATION OF LINE SPREAD FUNCTION

Starting with Artman's shift equation we seek to separate the effects of alignment error from the effects of refractive index that determine the critical angle:

$$D_\perp = \frac{\lambda}{\pi}\frac{\sin(\theta_i)}{\sqrt{\sin^2(\theta_i)-\sin^2(\theta_c)}},$$

$$D_\perp = \frac{\lambda}{\pi}\frac{\sin(\theta_i)}{\sqrt{\sin(\theta_i)+\sin(\theta_c)}\sqrt{\sin(\theta_i)-\sin(\theta_c)}}. \quad \text{(A1)}$$

We separate, regroup, and recollect terms to produce Eq. (A2):

$$D_\perp = \frac{\lambda}{\pi}\frac{\sin(\theta_i)}{\sqrt{2\sin\left(\theta_i+\frac{\delta}{2}\right)\cos\left(\theta_i+\frac{\delta}{2}\right)}\sqrt{\sin(\delta)}}. \quad \text{(A2)}$$

If $\theta_i \gg \delta$ and $\delta \ll 1$ then Eq. (A2) can be approximated by

$$D_\perp = \frac{\lambda}{\pi}\frac{1}{\sqrt{2\cot(\theta_i)}\sqrt{\delta}}. \quad \text{(A3)}$$

In the limit as $\delta \to 0$, $D_\perp \to \infty$. The dependence of shift on $\delta$ is now partially separated.

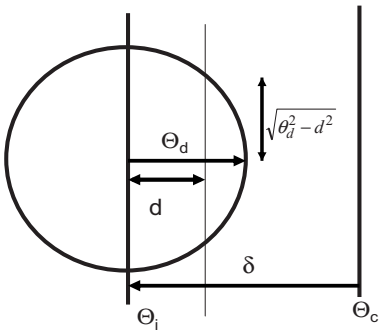


FIG. 7. Divergence cone geometry.

For a distributed source divergence represented by the circle above, the output shift becomes a function of position (d) in the cone of divergence. The Jacobian which relates the input $d$-space to the output $D_\perp$ space becomes the derivative of the shift function:

$$D_\perp = \frac{\lambda}{\pi}\frac{1}{\sqrt{2\cot(\theta_i)}\sqrt{\sin|\delta-d|}},$$

$$\frac{\Delta D_\perp}{\Delta d} = \frac{\lambda}{\pi}\frac{\cos|\delta-d|}{\sqrt{2\cot(\theta_i)}\sqrt{(\sin|\delta-d|)^3}}\ (\text{m/rad}), \quad \text{(A4)}$$

where $-\theta_d \leqslant d \leqslant \theta_d$.

The contours of constant angle of incidence can be graphically represented in the space of the divergence cone. Although they are in general circular arcs, they can be approximated as vertical line segments for all divergences of practical interest. This is because the actual arc length varies from the chordal length by the approximation $\sin(x) \cong x$, where $x$ is the divergence of the beam. Practical apparatus for exploiting this effect will use divergences of less than .01 radians and the errors will be on the order of $10^{-6}$. With this approximation in mind we construct a graphical representation of the segments of uniform shift that allows us to cast an intensity shift equation in the $d$ or divergence space (see Fig. 7).

The total energy in a vertical section of the divergence cone is simply the integral of the intensity in the vertical direction. We divide by the Jacobian [from Eq. (A4)] to obtain the intensity distribution as a function of shift position. For a uniform circular spot this becomes

$$I(D_\perp) = \frac{2I_0}{\pi\theta_d^2}\sqrt{\theta_d^2-d^2}\,\Delta d/\Delta D_\perp, \quad \text{(A5)}$$

$$I(D_\perp) = \frac{2I_0}{\lambda\theta_d^2}\sqrt{\theta_d^2-d^2}\sqrt{2\cot(\theta_i)}\frac{\sqrt{(\sin|\delta-d|)^3}}{\cos(\delta-d)}. \quad \text{(A6)}$$

This equation is now the shift distribution in the input $d$ space. To describe the intensity distribution in output or shifted space we must convert the $d$ variable to a $D_\perp$ variable. First we recast Artman's equation for direct substitution:

$$d = \delta - \lambda^2/\pi^2 D_\perp^2 2\cot(\theta_i)$$

$$\sqrt{\theta_d^2 - d^2} = \sqrt{\theta_d^2 - [\delta - \lambda^2/\pi^2 D_\perp^2 2\cot(\theta_i)]^2}$$
$$= \sqrt{\theta_d^2 - \delta^2 + \frac{\delta\lambda^2}{\pi^2 D_\perp^2 \cot(\theta_i)} - \frac{\lambda^4}{\pi^4 D_\perp^4 4\cot^2(\theta_i)}}, \quad \text{(A7)}$$

$$\theta_d^2 - d^2 = \theta_d^2 - \delta^2 + \frac{2\delta(\delta+\theta_d){D_{\perp\text{edge}}}^2}{D_\perp^2} - \frac{{D_{\perp\text{edge}}}^4(\delta+\theta_d)^2}{D_\perp^4}, \quad \text{(A8)}$$

where

$$D_{\perp\text{edge}} = \frac{\lambda}{\pi}\frac{1}{\sqrt{2\cot(\theta_i)}\sqrt{\sin(\theta_d+\delta)}}. \quad \text{(A9)}$$

From Eqs. (A4) and (A9)

$$\frac{D_{\perp\text{edge}}}{D_\perp} = \frac{\sqrt{\sin(\delta-d)}}{\sqrt{\sin(\theta_d+\delta)}},$$

$$\left(\frac{D_{\perp\text{edge}}}{D_\perp}\right)^3 \sqrt{\sin(\theta_d+\delta)^3} = \sqrt{\sin(\delta-d)^3}. \quad \text{(A10)}$$

In the limit as $\delta \to 0$ Eq. (A8) reduces to

$$\sqrt{\theta_d^2 - d^2} = \theta_d \sqrt{\left(1 - \frac{{D_{\perp\text{edge}}}^4}{D_\perp^4}\right)}. \quad \text{(A11)}$$

Combining this result with Eq. (A10) and letting $\delta \to 0$ yields

$$\lim_{\delta\to 0}[I(D_\perp)] = \frac{I_0}{\lambda}\sqrt{\theta_d}\frac{D_{\perp\text{edge}}^3}{D_\perp^3}\sqrt{1 - \frac{D_{\perp\text{edge}}^4}{D_\perp^4}}. \quad \text{(A12)}$$

Corrections to this approximation for $\delta \neq 0$ due to the quadratic term in Eq. (A8) can be obtained by altering the powers under the radical to noninteger values. This technique accounts well for the erratic behavior of the function when the alignment angle approaches the divergence angle. This produces the Green's function for shift distributions below divergence angle:

$$I_{\text{LSF}} = \frac{I_0}{\lambda\theta_d}\sqrt{2\cot(\theta_i)}\sqrt{[\sin(\theta_d+\delta)]^3} \times \sqrt{\left(\frac{D_{\perp\text{edge}}}{x}\right)^a - \left(\frac{D_{\perp\text{edge}}}{x}\right)^b},$$
$$x \geq D_{\perp\text{edge}}. \quad \text{(A13)}$$

To split the leading and trailing components of the shifted wave fronts in the region below divergence the sign of the shift angle $\delta$ must be taken into account. This minor adjustment is given in Eq. (8) of the text.

In the region where the magnitude of the alignment angle is greater than the magnitude of the divergence angle, Eqs. (A15a) and (A15b) give complete expressions for the shift distribution. For numerical calculations the form of Eq. (A6) combined with the positional conversion of Eq. (A4) is best suited for describing the shift distributions. When the shift angle is greater than the divergence angle the impulse response is bounded and the upper limit of $D_\perp$ is given by $D_{\perp_{\text{edge2}}}$ given in Eq. (A14):

$$D_{\perp\text{edge2}} = \frac{\lambda}{\pi}\frac{1}{\sqrt{2\cot(\theta_i)}\sqrt{\sin(\delta-\theta_d)}}. \quad \text{(A14)}$$

It should be noted for consistency that many of these equations are approximations based upon representing $\sin(x)$ as $x$. This approximation is very accurate when $x < 0.01$ radians. The expression for $\cot(\theta_i)$ is valid when $\delta$ is much smaller than $\theta_i$. This approximation breaks down when the source divergence is very large or when the angle of incidence becomes very small. The former case occurs when poorly collimated sources are used. The latter case occurs for large ratios of refractive index. A final condition occurs near grazing incidence where we must require that $\theta_i + \delta < \pi/2$:

$$I(D_\perp) = \frac{2I_0}{\lambda\theta_d^2}\sqrt{\theta_d^2 - \delta^2 + \frac{\delta\lambda^2}{\pi^2 D_\perp^2 \cot(\theta_i)} - \frac{\lambda^4}{\pi^4 D_\perp^4 4\cot^2(\theta_i)}} \times \sqrt{2\cot(\theta_i)}\left(\frac{D_{\perp\text{edge}}}{D_\perp}\right)^3 \sqrt{[\sin(\theta_d+\delta)]^3} \quad \forall\ \delta \quad \text{(A15a)}$$

or, alternately,

$$I(D_\perp) = I_0\frac{\lambda^2}{\pi^3\theta_d^2}\frac{1}{2\cot(\theta_i)}\frac{1}{D_\perp^3} \times \sqrt{\theta_d^2 - \delta^2 + \frac{\delta\lambda^2}{\pi^2 D_\perp^2 \cot(\theta_i)} - \frac{\lambda^4}{\pi^4 D_\perp^4 4\cot^2(\theta_i)}} \quad \forall\ \delta. \quad \text{(A15b)}$$

Equations (A15a) and (A15b) are both valid for $D_{\perp\text{edge}} \leq D_\perp \leq D_{\perp\text{edge2}}$ and the $\cos(\delta - d) \cong 1$ term has been suppressed for notational simplicity.

## APPENDIX B: DETECTABILITY LIMITS OF DIVERGENT MODEL

$$D_{\perp\text{edge}} \equiv S = \frac{\lambda}{\pi}\frac{1}{\sqrt{2\cot(\theta_i)}}\frac{1}{\sqrt{\sin(\theta_d+|\delta|)}},$$

$$\frac{dS}{dn} = \frac{dS}{d\theta_c}\frac{d\theta_c}{dn} = \frac{dS}{d\delta}\frac{d\delta}{dn},$$

$$\theta_i = \theta_c + \delta \quad \text{or} \quad \delta = \theta_i - \theta_c, \quad \text{(B1)}$$

$$\sin(\theta_c) = \frac{n_0}{n_1}, \quad \cos(\theta_c)d\theta_c = \frac{-n_0}{n_1^2}dn. \quad \text{(B2)}$$

If a change in $\delta$ results from a shift in refractive index the incidence angle remains constant:

$$\left.\frac{dS}{d\delta}\right|_{\theta_i=\text{const}} = \frac{-\lambda}{\pi}\frac{1}{\sqrt{2\cot(\theta_i)}}\frac{\cos(\theta_d+|\delta|)}{\sqrt{\sin^3(\theta_d+|\delta|)}}. \quad \text{(B3)}$$

For $\theta_d + \delta < 0.01$ we can approximate the expression to

$$\left.\frac{dS}{d\delta}\right|_{\theta_i=\text{const}} \cong \frac{-\lambda}{\pi}\frac{1}{\sqrt{2\cot(\theta_i)}}\frac{1}{\sqrt{(\theta_d+|\delta|)^3}}, \tag{B4}$$

$$\left.\frac{dS}{dn}\right|_{\theta_i=\text{const}} \cong \frac{\lambda}{\pi}\frac{1}{\sqrt{2\cot(\theta_i)}}\frac{1}{\sqrt{(\theta_d+|\delta|)^3}}\frac{n_0}{\cos(\theta_c)n_1^2}. \tag{B5}$$

For practical estimation, consider a fused silica to air interface at critical angle. $n_1 \simeq 1.4$, $\theta_c \simeq \frac{\pi}{4}$, and $\delta=0$:

$$\left.\frac{dS}{dn}\right|_{\theta_i=\theta_c^+} \cong \frac{\lambda}{\pi}\theta_d^{-3/2} \quad \text{(fused silica approximation)}.$$

If we define the detectability threshold for shift measurement as $T_s$ and the detectability threshold for refractive index variation as $T_n$ then, $T_n=\frac{T_s}{dS/dn}$, roughly proportional to $\theta_d^{3/2}$, i.e., a 10-fold improvement in divergent angle yields more than a 30-fold improvement in shift detection. To detect a change of $10^{-5}$ in refractive index of the air for $\theta_d=0.001$ would require resolving $D_{\text{edge}}$ to 0.015 pixels, i.e., $T_s=0.1\lambda$, which is common practice today.


[1] F. Goos and H. Hanchen, Ann. Phys. **6**, 333 (1947).
[2] I. Newton, *Optick* (Dover, London, 1952).
[3] J. D. Jackson, *Classical Electrodynamics*, 3rd ed. (John Wiley and Sons, New York, 1999).
[4] H. K. V. Losch, Optik (Stuttgart) **37**, 160 (1970); **32**, 190 (1970); **32**, 553 (1971).
[5] L. de Broglie and J. P. Vigier, Phys. Rev. Lett. **28**, 1001 (1972).
[6] G. J. Troup, J. L. A. Francey, R. G. Turner, and A. Tirkel, Phys. Rev. Lett. **28**, 1540 (1972).
[7] B. R. Horowitz and T. Tamir, J. Opt. Soc. Am. **61**, 586 (1971).
[8] A. Puri and J. L. Birman, J. Opt. Soc. Am. A **3**, 543 (1986).
[9] V. M. Antar and W. M. Boerner, Can. J. Phys. **32**, 962 (1973).
[10] F. Bretenaker, A. Floch, and L. Dutraiux, Phys. Rev. Lett. **68**, 931 (1992).
[11] X. Yin, L. Hesselink, Z. Liu, N. Fang, and X. Zhang, Appl. Phys. Lett. **85**, 372 (2004).
[12] B-E. Moshe, A. Zomet, and S. K. Nayar, IEEE Trans. Pattern Anal. Mach. Intell. **27**, 980 (2005).
[13] R. Micheletto, Y. Kawakawi, K. Hamamoto, and S. Kawai, Opt. Lett. **31**, 205 (2006).
[14] M. Kisworo, S. Ventkatesh, and G. West, IEEE Trans. Pattern Anal. Mach. Intell. **16**, 405 (1994).